

A Unified Remote Sensing Anomaly Detector Across Modalities and Scenes via Deviation Relationship Learning

Jingtao Li, Xinyu Wang*, Hengwei Zhao, Liangpei Zhang, Fellow, IEEE, and Yanfei Zhong, Senior Member, IEEE

Abstract—Remote sensing anomaly detector can find the objects deviating from the background as potential targets. Given the diversity in earth anomaly types, a unified anomaly detector across modalities and scenes should be cost-effective and flexible to new earth observation sources and anomaly types. However, the current anomaly detectors are limited to a single modality and single scene, since they aim to learn the varying background distribution. Motivated by the universal anomaly deviation pattern, in that anomalies exhibit deviations from their local context, we exploit this characteristic to build a unified anomaly detector. Firstly, we reformulate the anomaly detection task as an undirected bilayer graph based on the deviation relationship, where the anomaly score is modeled as the conditional probability, given the pattern of the background and normal objects. The learning objective is then expressed as a conditional probability ranking problem. Furthermore, we design an instantiation of the reformulation in the data, architecture, and optimization aspects. Simulated spectral and spatial anomalies drive the instantiated architecture. The model is optimized directly for the conditional probability ranking. The proposed model was validated in five modalities—hyperspectral, visible light, synthetic aperture radar (SAR), infrared and low-light—to show its unified detection ability.

Index Terms—Anomaly detection in remote sensing, transferability, cross-modality and cross-scene, unified detector

1. INTRODUCTION

Remote sensing images can be used to monitor anomalies on the Earth’s surface in a large-scale and consistent space [1]. Remote sensing anomalies are generally defined as pixels deviating from the background spectrally or spatially, which are detected without any prior knowledge [2]. The anomalies vary in category and electromagnetic response. For example, landslide anomalies exhibit a response in the visible and radar range, while fire anomalies are mainly related to the thermal infrared spectra [3]. Anomalies caused by environmental pollution quantitatively relate to responses across ultraviolet, visible, infrared, and microwave spectra [3]. Given the diversity in anomaly types and responses across modalities, a unified model across modalities and scenes should be cost-effective and allow easy adaptation to new data sources and anomaly types.

Designing a unified anomaly detector is challenging due to

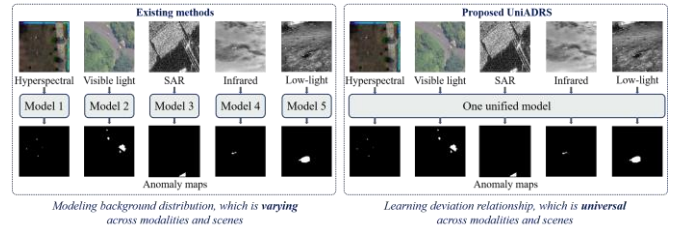


Fig. 1. The comparison between the existing models and the proposed UniADRS. Existing models focus on background modeling. Since the background distribution is varying, they need to be trained for each modality and scene. In contrast, UniADRS leverages the universal deviation relationship between the anomalies and the background to build a unified detector in an unsupervised manner.

the difference in imaging mechanisms and the varying scene distributions. For example, the hyperspectral modality can record a continuous spectrum from visible to short-wave infrared [4], and thus the acquired imagery always has hundreds of channels for precise recognition [5], [6]. In contrast, the synthetic aperture radar (SAR) modality is a side-looking radar that records the received echoes coherently [7], [8], providing more structural information with several channels. Large-scale scenes encompass diverse backgrounds, including forests, urban areas, and oceans, with highly variable distributions [9], [10]. A unified detector therefore needs to be robust with regard to these modality and scene differences.

The current anomaly detection methods are still limited to a single modality and single scene since they aim to learn the varying background distribution. They focus on describing a certain background distribution with a statistical-based [11]–[16], representation-based [17]–[20], or deep learning based method [21]–[26]. The statistics-based methods describe the background distribution with statistical techniques [11], where the likelihood implies the anomaly degree. However, the built distribution can only describe limited scenes. The representation-based methods construct the detector considering the prior properties of the anomalies and the background, such as the low-rank and sparsity [2], [27]. These methods always build a background dictionary for each scene. The deep learning based models are trained to reconstruct the

Jingtao Li, Hengwei Zhao, Liangpei Zhang, and Yanfei Zhong are with the State Key Laboratory of Information Engineering in Surveying, Mapping and Remote Sensing and the Hubei Provincial Engineering Research Center of Natural Resources Remote Sensing Monitoring, Wuhan University, Wuhan 430072, China. (e-mail: jingtaoli@whu.edu.cn; whu_zhaohw@whu.edu.cn; zlp62@whu.edu.cn; zhongyanfei@whu.edu.cn).

Xinyu Wang is with the School of Remote Sensing and Information Engineering, Wuhan University, Wuhan 430072, China (*Corresponding author, e-mail: wangxinyu@whu.edu.cn).

background and assume that the normal pixels have a smaller reconstruction error than the anomaly ones [28]–[30]. However, a new model needs to be trained for an unseen scene. It can be seen that all of these methods attempt to describe only the background distribution from the original pixels to deep features, with additional priors or constraints. However, the background always varies and the constructed detector cannot be transferred. This is the core reason why the existing models need to be constructed again for each modality and scene.

Motivated by the universal anomaly deviation pattern, in that anomalies exhibit noticeable deviations from their local context [12], [24], [29], [31], we propose to leverage this consistent deviation relationship to build a unified detector (see Fig. 1). The key insight is that, while the background distribution can vary across modalities and scenes, this deviation pattern persists. Unlike traditional background modeling methods which focus on the distribution of the background only, the deviation relationship concerns the relational difference between the pixel and its surrounding context. We hypothesize that, by detecting anomalies based on modeling the deviation relationship, the unified detector could maintain a robust performance across varying modalities and scenes.

Based on the deviation relationship, the anomaly detection task is first reformulated as an undirected bilayer graph. Given the pixel descriptors in the first layer and the normal descriptors in the second layer, the anomaly map can be represented as the edge probability. Specifically, the anomaly score of each pixel is modeled as the conditional probability given the pattern of the background and normal objects, due to their ranking consistency and the background-independent property. Ranking consistency means a normal pixel has a higher conditional probability than anomaly pixels, where the anomaly score ranking is equivalent to the probability ranking. The background-independent property likely shows that the conditional probability is independent of the modality and the scene itself. The learning objective can be further expressed as a conditional probability ranking problem. The task reformulation provides the theoretical guidance for the unified model design.

Furthermore, an instantiation of the reformulated form is designed in the data, architecture, and optimization aspects. Anomaly samples in the spectral domain and spatial domain are simulated, respectively, to make the detection model general and follow a one-step detection paradigm [29]. For each sample, the background, normal objects, and anomaly objects are explicitly simulated following the reformulated form. The model architecture is built corresponding to the bilayer undirected graph, where the layer nodes are instantiated as deep features and the anomaly map is the final output. Normal features are obtained with spatial downsampling to remove anomalies and with the encoder-decoder paradigm to be discriminative. Given the simulated anomaly labels and the output anomaly map, the model is optimized for the anomaly detection task directly, without any surrogate objective. Specifically, the expansion form and the plain form of the conditional probability ranking targets are implemented as the feature-level and pixel-level optimization, respectively. The feature-level optimization uses the enclosing hypersphere to

describe the compactness, inspired by the energy function of the restricted Boltzmann machine (RBM). The pixel-level optimization aims to make the ranking metric (i.e., the area under the curve (AUC)) differentiable. This instantiated model is named **unified anomaly detection in remote sensing (UniADRS)**. UniADRS was validated in the five modalities of hyperspectral, visible light, SAR, infrared, and low light, to show its cross-modal ability. The low-light dataset was captured and labeled by the authors. Each modality had varying scenes, to show the cross-scene ability of the proposed model.

The main contributions of this paper can be summarized as follows.

- 1) Based on the universal deviation relationship of the anomalies and background, the anomaly detection task is reformulated with a bilayer undirected graph for the advantage in relationship expression and transformed into a conditional probability ranking problem. The task reformulation provides the theoretical guidance for the unified model design.
- 2) An instantiation of the reformulated form is designed in the data, architecture, and optimization aspects. A simulated strategy for samples in the spectral domain and spatial domain is designed, where numerous anomaly objects, normal objects and background are simulated. The model architecture is built upon the bilayer undirected graph.
- 3) The instantiated model is optimized for the anomaly detection task directly, where the expansion form and the plain form of the conditional probability ranking targets are implemented as the feature-level and pixel-level optimization, respectively. Without surrogate targets, they work together and are superior to the mainstream classification objectives.

The rest of this paper is organized as follows. Section 2 introduces the related work in anomaly detection in different domains. Section 3 provides a detailed description of the task reformulation and the instantiated model. Section 4 gives the experimental results and analysis. Finally, the paper is concluded in Section 5. The code is available at <https://github.com/Jingtao-Li-CVer/UniADRS>.

2. RELATED WORK

2.1 Anomaly Detection in Remote Sensing

Anomaly detection in remote sensing (ADRS) involves finding the objects that are anomalous to the background, without any prior information [32]. There is not an unambiguous way to define an anomaly, which is generally identified as an observation deviating from the background, spectrally or spatially [2]. In fact, the category of the anomalies depends on the particular application. The anomalies can be the camouflage [44] or vehicles in military surveillance [33], rare minerals in geological detection [34], infected trees in forestry [35], and ships on the sea [34]. Since the ADRS methods do not use any prior knowledge, they cannot distinguish between real anomalies and detections that are not of interest. The detection

result is often a first step, which provides the potential targets for the subsequent recognition [36].

Readers may wonder why we do not train a supervised target detector directly. There are two main reasons for this. Firstly, the training samples are difficult to obtain for some targets (e.g., military camouflage) and some modalities (e.g., hyperspectral). Secondly, an ADRS can detect unknown objects out of the preset category system, which is important for some applications such as Mars exploration.

Some fields may seem similar to the ADRS methods, but there are significant differences. Anomaly detection in medical or industrial images finds the anomaly pattern given a set of normal samples [37], where the normal pattern is no longer the background defined in the ADRS. The detected anomalies have both large and small areas. Despite some researchers having defined the normal pattern as the same as the industrial one in high-resolution optical images [35], we inherit the classical anomaly definition in the remote sensing community and treat the background as the normal pattern in each scene. Compared to tiny object detection [38], [39], an ADRS considers an open-set setting without preset categories. In addition, the anomalies in an ADRS are always small and rare, while tiny object detection also considers abundant small objects (e.g., cars in a parking lot).

Currently, most ADRS methods aim to extract the discriminative background features and then use a distance metric to assign the anomaly score for each pixel. Depending on whether spectral information is available or not, the ADRS methods can be divided into the spectral domain (e.g., hyperspectral, multispectral) and the spatial domain (e.g., optical, SAR, infrared, LiDAR points).

2.2 Anomaly Detection in the Spectral Domain

Anomaly detection in the spectral domain is a hot spot in the remote sensing community. According to the difference of the basic principle, the models can be further divided into three categories: statistical-based [11]–[16] models, representation-based [17]–[20] models, and deep learning based method [21]–[26].

Statistics-based models. This statistical models aim to describe the background distribution with statistical techniques [12], where the likelihood implies the anomaly degree. For example, the classic Reed-Xiaoli (RX) detector models the background as a multivariate Gaussian distribution [13]. The Mahalanobis distance between the test pixel and the modeled distribution is then treated as the anomaly degree. Inspired by the RX detector, many improved variants have been proposed. For example, Nasrabadi *et al.* [14] devised the kernel RX detector (KRX) to enhance the spectral separability with kernel transformation. In addition, the subspace RX (SSRX) detector was designed by Schaum *et al.* [40] to eliminate noise contamination. Except for the accuracy improvement, some researchers have focused on real-time processing with RX detectors [15], [41], [42]. To address the difficulty of determining the distribution form, statistical cluster centers and decision hyperspheres have also been deployed [43], [44].

Despite the statistical methods having a clear mathematical basis, the constructed distribution is only suitable for single images [29] and does not have the ability to be cross-modal or cross-scene.

Representation-based models. The representation-based models construct the detector considering the prior properties of the anomalies or background [17], [45], and include sparsity, collaborative, and low-rank based detectors. Ling *et al.* [18] constructed a sparsity-based detector with the sum-to-one and non-negativity constraints, making the detector less sensitive to the anomalies. Differing from sparse representation, collaborative representation assumes that the background pixels can be reconstructed by the surrounding pixels while the anomalies cannot [19]. The classic collaborative representation detector (CRD) follows this assumption [20]. To make full use of the global structural information (i.e., low-rank property), the low-rank and sparse matrix decomposition model (LSDM) was designed by decomposing the hyperspectral image into a low-rank background and sparse anomalies [17]. Sun *et al.* [46] implemented the LSDM technique with robust principal component analysis (RPCA) [47]. Zhang *et al.* [48] proposed a detector based on the low-rank and sparse matrix decomposition (LRaSMD) technique and applied the Mahalanobis distance to estimate the background part (LSMAD). Xu *et al.* [49] first introduced the background dictionary and proposed a detector based on low-rank and sparse representation (LRASR).

Deep learning based models. Most deep learning based models follow a two-step paradigm [29], where they assume that the normal pixels have a smaller reconstruction error with the deep model than the anomaly ones. Li *et al.* [22] first introduced a convolutional neural network (CNN) into the hyperspectral anomaly detection (HAD) task in a supervised way. To detect anomalies according to a practical situation, some unsupervised methods have been proposed. For example, Xie *et al.* [25] proposed the spectral constrained adversarial autoencoder (SC_AAE), where a spectral constraint strategy is incorporated for better latent representation. However, these methods always involve complicated manual parameter setting and preprocessing steps. To this end, Wang *et al.* [50] proposed the autonomous hyperspectral anomaly detection network (Auto-AD) with an adaptive-weighted loss function, where a high reconstruction error implies anomaly. Except for the autoencoder model, generative adversarial network (GAN)-based models have also been used, where the generation error from real images is treated as the anomaly degree [51]–[53]. For example, Jiang *et al.* [53] introduced a semi-supervised GAN with dual RX detector to learn the discriminative reconstruction of background and anomalies. Inspired by the fact that both the autoencoder-based models and GAN-based models adopt the reconstruction proxy task and need to be trained for each image, Li *et al.* [29] proposed the one-step detection paradigm and transferred direct detection (TDD) model, where the proxy task is abandoned and the trained model

can be transferred to unseen images directly. However, the TDD model is still limited in the hyperspectral modality.

2.3 Anomaly Detection in the Spatial Domain

Studies in the spatial domain are relatively few in number, and mainly consider optical images [54], SAR images [21], [31], thermal images [24], [55], and LiDAR point cloud data [23], [56]. For the optical modality, Wang *et al.* [54] proposed a coarse-to-fine ship detection strategy based on anomaly detection and spatial pyramid pooling PCANet (SPP-PCANet), where the effectiveness was validated using GF-1 and GF-2 images. For the SAR modality, Haitman *et al.* [31] used both the RX detector and the non-negative matrix factorization (NNMF) learning algorithm for an adaptive detection threshold and detected the sludge pools of the Shafdan wastewater treatment plant in Israel. Muzeau *et al.* [21] considered the speckle noise problem of SAR images and designed a self-supervised algorithm for vehicle detection. For the thermal modality, Lile *et al.* [24] developed a detection framework based on the VGG-16 model for electrical preventive maintenance application. Sledz *et al.* [55] formulated the thermal anomaly detection task as a salient region detection task and presented a two-step detection method. For the LiDAR modality, Shimoni *et al.* [56] fused LiDAR data and hyperspectral data and proposed a method based on shape/spectral integration (SSI) decision-level fusion for vehicle detection in shadowed areas. Shin *et al.* [23] combined LiDAR data and thermal data to detect both elevation and temperature anomalies for robot surveillance application. However, similarly, the detection methods in the spatial domain are also limited to a single modality and a single scene.

3. A UNIFIED REMOTE SENSING ANOMALY DETECTOR ACROSS MODALITIES AND SCENES

In this section, we first reformulate the ADRS task as an undirected bilayer graph and the learning target as conditional probability ranking based on the deviation relationship (Section 3.1), where the deviation degree (i.e., anomaly score) is modeled as the conditional probability. Furthermore, the task reformulation is instantiated, including sample simulation, model architecture, and optimization process (Section 3.2). The instantiated model is named **unified anomaly detection in remote sensing (UniADRS)**.

3.1 Anomaly Detection Task Reformulation Based on the Deviation Relationship

The traditional mathematical formulations, such as the statistical hypothesis test and low-rank decomposition, focus on background construction, and are lacking in generalization ability for varying modalities and scenes. We observed that the deviation relationship between anomalies and background is emphasized in all modalities and scenes [24], [29], [31], [57]. The concept of “deviation” refers to the relationship of two entities rather than only background. The deviation relationship remains unchanged for different modalities and scenes, which inspired us to design a unified detector.

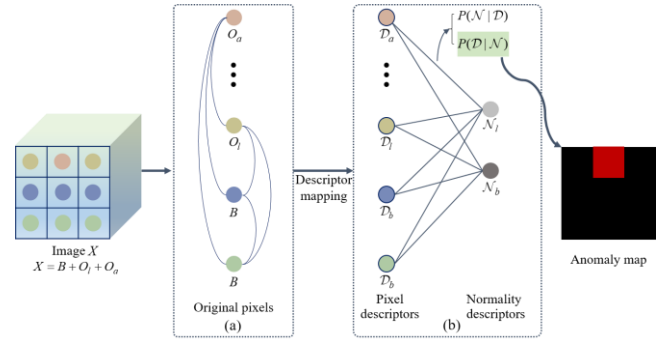


Fig. 2. The reformulated anomaly detection task in the form of bilayer undirected graph. The pixel descriptors \mathcal{D} in the first layer are aggregated and encoded into a much smaller number of normality descriptors \mathcal{N} . The deviation relationship of anomalies from background B and large normal objects O_l is modeled as the conditional probability given normal patterns (i.e. $P(\mathcal{D}|\mathcal{N})$ in (b)) due to the ranking consistency and the background-independent property.

3.1.1 Deviation Relationship in Reformulated Anomaly Detection Task

Formally, the remote sensing image X consists of the background B , the normal large objects O_l , and the anomaly objects O_a , as shown in Eq. (1), covering modalities with a high spectral resolution or spatial resolution.

$$X = B + O_l + O_a \quad (1)$$

Compared with the traditional methods, the focus is transformed from $P(B, O_l)$ to $P(O_a | (B, O_l))$. $P(O_a | (B, O_l))$ doesn't care about single O_a or (B, O_l) , but their relationship. Some prior studies may include O_l in B [49], [50]. Differently, we denote and model O_l explicitly in this paper, which brings stable promotion as shown in Section 4.3.1.

To represent the relationship in the detection workflow, a graph model is used to reformulate the anomaly detection task, as shown in Fig. 2. Although each original pixel $X_i \in X$ can be naturally considered as a graph node, the context dependences make the node connection have many intractable rings, as shown in Fig. 2(a). To make the problem tractable, we decompose the dependencies by mapping each original pixel X_i into a descriptor \mathcal{D}_i containing contextual features, as shown in Fig. 2(b). In practice, we can construct a stem block (based on a CNN or transformer) to encode the contextual information and complete the decomposition process. The obtained descriptor cube \mathcal{D} has the same spatial size as $H \times W$ with X , and each descriptor acts as a graph node.

After the descriptor mapping process, a bilayer undirected graph is constructed, as shown in Fig. 2(b). The pixel descriptors \mathcal{D} in the first layer are aggregated and encoded into a much smaller number of normality descriptors \mathcal{N} in the second layer, which includes the normal background \mathcal{N}_b and normal large objects \mathcal{N}_l . Anomaly objects are ignored when

obtaining \mathcal{N} , due to their rarity. The undirected dense connection is built between the two layers under the fact that no prior information can reduce the edge dependence.

Each undirected edge represents two dependencies: $P(\mathcal{N}|\mathcal{D})$ and $P(\mathcal{D}|\mathcal{N})$. $P(\mathcal{N}|\mathcal{D})$ represents the normality descriptor extraction process. $P(\mathcal{D}|\mathcal{N})$ implies the occurrence probability of each pixel descriptor, given \mathcal{N} . Considering that anomaly descriptors have less correlation with \mathcal{N}_b and \mathcal{N}_l , their $P(\mathcal{D}|\mathcal{N})$ should be smaller than the value of the normal pixel descriptors, which has consistency with the ranking of the anomaly scores. Furthermore, $P(\mathcal{D}|\mathcal{N})$ can be proven to be independent of the modality and the scene itself. If we set α to be the unique characteristics of any modality and scene (e.g., the speckle noise in SAR imagery), Eqs. (2) and (3) hold due to the independence of α from \mathcal{D} and \mathcal{N} .

$$P(\mathcal{D}|\mathcal{N}) = P(\mathcal{D}|\mathcal{N}, \alpha) \quad (2)$$

$$P(\alpha|\alpha) = P(\alpha|\mathcal{N}, \alpha) \quad (3)$$

Furthermore, Eq. (4) shows that α has no effect on the computation of the final $P(\mathcal{D}|\mathcal{N})$, based on Eqs. (2) and (3). Therefore, due to the advantages of ranking consistency with the anomaly score, the background-independent $P(\mathcal{D}|\mathcal{N})$ is treated as the deviation degree (i.e., anomaly score) directly in the bilayer graph.

$$\begin{aligned} P((\mathcal{D}, \alpha)|\mathcal{N}, \alpha) \\ &= P(\mathcal{D}|\mathcal{N}, \alpha) * P(\alpha|\mathcal{N}, \alpha) \\ &= P(\mathcal{D}|\mathcal{N}) * P(\alpha|\alpha) \\ &= P(\mathcal{D}|\mathcal{N}) \end{aligned} \quad (4)$$

3.1.2 Conditional Probability Ranking Target

Furthermore, the optimization objective for the ADRS task can be expressed as shown in Eq. (5), where \mathcal{D}_n represents the normal descriptors in \mathcal{D} and \mathcal{D}_a represents the anomaly ones. Equation (5) optimizes the anomaly score directly and aims to increase the score separability of \mathcal{D}_n and \mathcal{D}_a :

$$\max(P(\mathcal{D}_n|\mathcal{N}) - P(\mathcal{D}_a|\mathcal{N})) \quad (5)$$

\mathcal{D}_n can be further decomposed into normal background \mathcal{D}_b and normal large objects \mathcal{D}_l in the first layer. If we substitute \mathcal{D}_n and \mathcal{N} with the decomposed factors, we can obtain Eqs. (6) and (7):

$$P(\mathcal{D}_n|\mathcal{N}) = P((\mathcal{D}_b, \mathcal{D}_l)|(\mathcal{N}_b, \mathcal{N}_l)) \quad (6)$$

$$P(\mathcal{D}_a|\mathcal{N}) = P(\mathcal{D}_a|(\mathcal{N}_b, \mathcal{N}_l)) \quad (7)$$

If we rewrite Eqs. (6) and (7) following the Bayes' theorem and

remove the common denominator factor, Eq. (5) can be transformed, as shown in Eq. (8):

$$\max(P((\mathcal{D}_b, \mathcal{D}_l), \mathcal{N}_b, \mathcal{N}_l) - P(\mathcal{D}_a, \mathcal{N}_b, \mathcal{N}_l)) \quad (8)$$

Considering the independence of nodes within layers, the constructed bilayer undirected graph in Fig. 2(b) is also a kind of RBM [58]. From the view of the RBM, the probability can be re-written in energy-based form, as shown in Eq. (9), where Z_1 is the partition function. The RBM implements the energy function as shown in Eq. (10) with learned parameters b , c , and W given two layer variables v and h . To make Eq. (10) more suitable for the modern deep learning technique, we abstract the three terms with non-specific functions and rewrite it as E_a , as shown in Eq. (11). M_1 , M_2 , and M_3 can be instantiated as a deep network module, which focuses on the compactness according to the demand of the clique potential function.

$$P((\mathcal{D}_b, \mathcal{D}_l), \mathcal{N}_b, \mathcal{N}_l) = \frac{1}{Z_1} \exp(-E((\mathcal{D}_b, \mathcal{D}_l), \mathcal{N}_b, \mathcal{N}_l)) \quad (9)$$

$$E(v, h) = -b^T v - c^T h - v^T W h \quad (10)$$

$$E_a(v, h) = -M_1(v) - M_2(h) - M_3(v, h) \quad (11)$$

With the abstract energy function in Eq. (11), Eq. (9) can be transformed into Eq. (12). Similarly, $P(\mathcal{D}_a, \mathcal{N}_b, \mathcal{N}_l)$ can be rewritten as shown in Eq. (13).

$$\begin{aligned} P((\mathcal{D}_b, \mathcal{D}_l), \mathcal{N}_b, \mathcal{N}_l) &= \frac{1}{Z_1} \exp(M_1(\mathcal{D}_b, \mathcal{D}_l)) \\ &+ M_2(\mathcal{N}_b, \mathcal{N}_l) + M_3(\mathcal{D}_b, \mathcal{D}_l, \mathcal{N}_b, \mathcal{N}_l) \end{aligned} \quad (12)$$

$$\begin{aligned} P(\mathcal{D}_a, \mathcal{N}_b, \mathcal{N}_l) &= \frac{1}{Z_2} \exp(M_1(\mathcal{D}_a)) \\ &+ M_2(\mathcal{N}_b, \mathcal{N}_l) + M_3(\mathcal{D}_a, \mathcal{N}_b, \mathcal{N}_l) \end{aligned} \quad (13)$$

In view of $M_2(\mathcal{N}_b, \mathcal{N}_l)$ having a synchronous effect on $P((\mathcal{D}_b, \mathcal{D}_l), \mathcal{N}_b, \mathcal{N}_l)$ and $P(\mathcal{D}_a, \mathcal{N}_b, \mathcal{N}_l)$ in Eq. (8), we can eliminate this for obtaining practical guidance when substituting Eqs. (12) and (13) into Eq. (8), and Eq. (14) can be obtained as follows:

$$\begin{aligned} \max\left(\frac{1}{Z_1} \exp(M_1(\mathcal{D}_b, \mathcal{D}_l) + M_3(\mathcal{D}_b, \mathcal{D}_l, \mathcal{N}_b, \mathcal{N}_l)) \right. \\ \left. - \frac{1}{Z_2} \exp(M_1(\mathcal{D}_a) + M_3(\mathcal{D}_a, \mathcal{N}_b, \mathcal{N}_l))\right) \end{aligned} \quad (14)$$

Equation (14) gives the final optimization objective of the anomaly detection reformulation, where $P(\mathcal{D}|\mathcal{N})$ is treated as the anomaly score, rather than $P(\mathcal{N})$ in most research. Equation (14) emphasizes the compactness learning, where

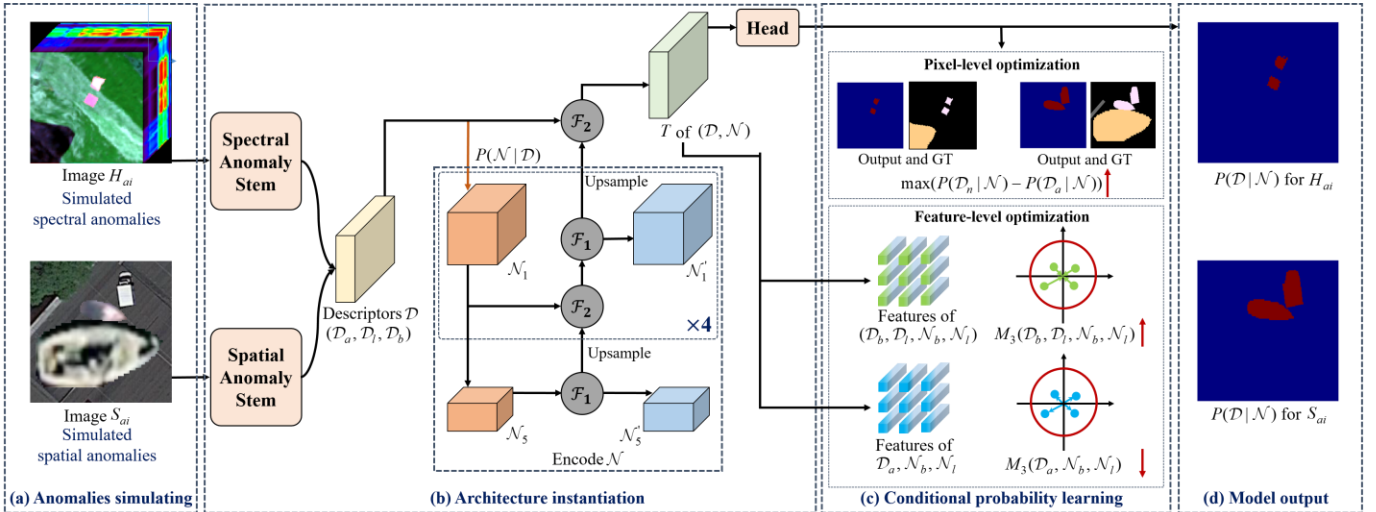


Fig. 3. The instantiated model according to the constructed bilayer undirected graph (Fig. 2). (a) Spectral and spatial anomalies are simulated by explicitly modeling the B , O_l and O_a with designed data argument workflows. Numerous simulated samples drive the model training end to end. (b) Model architecture instantiated the \mathcal{D} , \mathcal{N} , $P(\mathcal{N}|\mathcal{D})$, and $P(\mathcal{D}|\mathcal{N})$ as different modules, where $P(\mathcal{D}|\mathcal{N})$ is the outputting anomaly map. (c) By converting the deviation relationship learning problem as the conditional probability ranking as in Section 3.1.1, it is directly optimized in both pixel-level and feature-level without any surrogate loss. The instantiated model serves for the ADRS task in data, architecture and optimization aspects. (d) Instantiated model can output the anomaly maps directly without any post-processing step.

$(\mathcal{D}_b, \mathcal{D}_l, \mathcal{N}_b, \mathcal{N}_l)$ should be more compact than $(\mathcal{D}_a, \mathcal{N}_b, \mathcal{N}_l)$. This heuristic will subsequently help the optimization of the detection model.

3.2 Instantiated Anomaly Detection Model

The reformulated detection workflow and corresponding conditional learning target are instantiated in the data, architecture, and optimization aspects, as shown in Fig. 3.

3.2.1 Sample Simulation for Spectral and Spatial Anomalies

We follow the one-step detection paradigm [29] and the undirected graph model in Section 3.1 to simulate the anomaly samples. The one-step detection paradigm outputs the anomaly map directly and is trained using paired simulated samples in a supervised manner, obtaining a great detection ability and transferability. However, the simulation strategy in [29] does not fit our reformulation well because it considers B and O_l together and limits the transferability in a complex background (as shown in the experimental results obtained on the WHU-Hi dataset). In contrast, we explicitly simulate B , O_l , and O_a according to Eq. (14).

To simulate samples that are suitable for the cross-modal detection, we divide all the anomaly types into spectral anomalies and spatial anomalies. Spectral anomalies deviate from the surroundings with a large spectral difference, as seen in the hyperspectral modality. Spatial anomalies deviate in terms of the spatial features for the modality with few channels, such as the SAR and single-band thermal infrared modalities. Thus, the explicit simulation of B , O_l , and O_a in view of both the spectral anomalies and spatial anomalies is our core simulation strategy.

Spectral anomaly simulation. An unlabeled hyperspectral image is used to simulate the spectral anomalies, due to its high spectral resolution. Fig. 4 shows the simulation workflow. It is worth noting that the workflow input is the hyperspectral patch H cropped from the large-scale scene since the anomalies are defined in a local area. H is assumed to be anomaly-free due to the rarity property of anomalies. The π_1 operation randomly selects generation positions for O_l (yellow area) and O_a (pink area) from H to obtain H_l . Area control is important in the π_1 operation, where the areas of O_l and O_a should be within the preset range, to be consistent during the training stage. O_l occupies more area than O_a , and the remaining area in H is treated as B . In parallel with the π_1 operation, H is shuffled in the channel dimension to obtain H_{cs} , as shown in Fig. 4, which is considered as a spectrally deviating scene compared to H . The φ_1 operation then copies the pixel values of O_l and O_a from H_{cs} and pastes them into H_l , as shown in Eq. (16). In the obtained H_{cp} , the simulated O_l and O_a obey the deviation relationship, and the occurrence probability is consistent with the ranking of the corresponding $P(\mathcal{D}^p | \mathcal{D}^n)$.

$$H_{cp} = \varphi_1(H_{cs}, H_l) \quad (16)$$

Given that the selected location in H_{cp} is a regular square while real objects have diverse shapes, affine transformation is finally carried out to make the boundary of O_l and O_a more complex. Finally, the resulting spectral anomaly sample (i.e., H_{ai} and

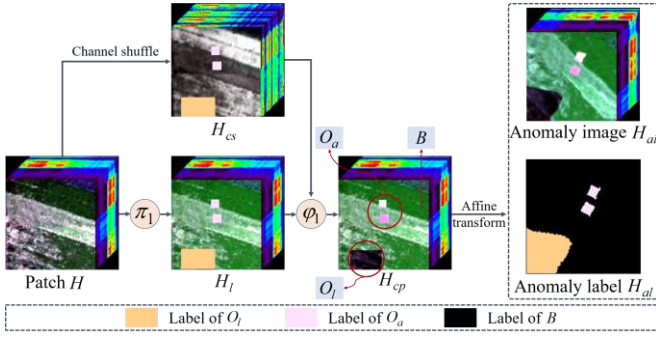


Fig. 4. The designed workflow for the spectral anomaly simulation, where O_a and O_l are simulated by shuffling the spectral channels in different area sizes. Affine transform is used to make the boundary more complex and realistic.

H_{al}) explicitly simulates B , O_l , and O_a with deviation relationship and complex shape. This workflow can generate numerous anomaly samples under the high randomness of each step.

Spatial anomaly simulation. A high-resolution instance segmentation dataset is used to simulate the spatial anomalies. The overall workflow is shown in Fig. 5. The high-resolution remote sensing dataset provides scenes with rich spatial details, which helps the model learn the complex spatial distribution. An instance segmentation dataset is chosen because the provided object labels allow us to obtain a noiseless B , O_l , and O_a . We used the iSAID dataset in this study [59]. For each input image S , we first masked out all the objects in S according to the original labels, which are denoted as the gray pixels in preprocessed label S_l . The remaining valid pixels in S are considered as B . To simulate O_l and O_a within the preset range, as mentioned before, an object bank is built separately, which contains a large number of different types of objects. In this study, we built the object bank with more than 650,000 instances from the iSAID dataset. For S , a certain number of objects are randomly selected from the object bank to act as O_l and O_a . Fig. 5 shows an example where three objects are chosen. The π_2 operation then separates the selected objects into two groups (O_l and O_a) and resizes them into the preset range. Next, the φ_2 operation pastes the resized O_l and O_a into S , and obtains the anomaly image S_{ai} . The corresponding label S_{al} can also be obtained. Equation 17 shows the mapping relationship of φ_2 :

$$S_{ai} = \varphi_2(S, O_l, O_a) \quad (17)$$

The large number of combinations between the object in the object bank and the input S can generate countless anomaly samples for feeding into the instantiated model (as shown in Fig. 3(a)). These samples help prevent the model from learning anomalies with specific context, and have stronger generalization for unknown scenes.

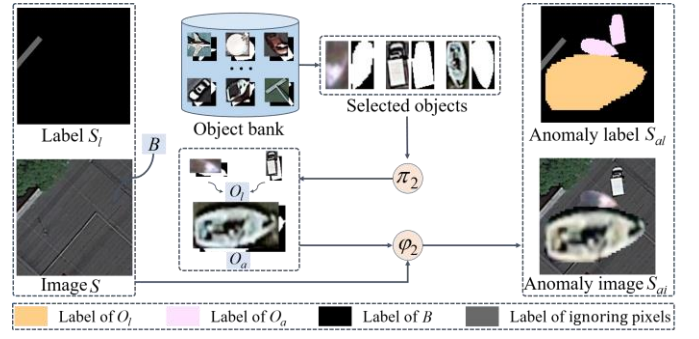


Fig. 5. The designed workflow for the spatial anomaly simulation, where O_a and O_l are selected randomly from the pre-made object bank and pasted into S by the φ_2 operation. The original objects in S are masked to be ignored.

3.2.2 Instantiated Network Architecture

According to the bilayer undirected graph, an instantiated network architecture is constructed (as shown in Fig. 3(b)). Specifically, we instantiate \mathcal{D} , \mathcal{N} , $P(\mathcal{N}|\mathcal{D})$, and $P(\mathcal{D}|\mathcal{N})$.

\mathcal{D} is the mapping pixel descriptor with context information, which acts as the preprocessing step in the reformulated workflow. Considering that the simulated anomalies are divided into spectral anomalies and spatial anomalies, two corresponding stems are designed to obtain \mathcal{D} . The spatial stem consists of two convolutional layers with kernel size 3×3 , followed by instance normalization and rectified linear unit (ReLU) activation. \mathcal{D} has the same spatial size as X , to prevent losing the spatial details of the anomalies, considering their low ratio property. The spectral stem is weighted-shared with the spatial stem so that they converge together. These two stems convert either the spatial anomaly samples or the spectral anomaly samples into the common descriptor form \mathcal{D} .

\mathcal{N} is encoded with five cascades of multi-level features, where the encoder-decoder paradigm is used. $\mathcal{N}_1 - \mathcal{N}_5$ represent the features in the encoder part, and $\mathcal{N}'_1 - \mathcal{N}'_5$ represents the corresponding decoder part. $\mathcal{N}_1 - \mathcal{N}_5$ is considered to contain only the features of O_l and B because they are obtained by significantly downsampling X . During the downsampling stage, the low proportion O_a is very likely to be eliminated. To fuse the multi-level features and obtain representative normal features, two fusion operations— \mathcal{F}_1 and \mathcal{F}_2 —are designed (as shown in Fig. 3(b)). Taking \mathcal{N}_5 as an example, the \mathcal{F}_1 operation can be expressed as shown in Eq. (18), where the local attention module (LAM) from [29] is used:

$$\mathcal{F}_1(\mathcal{N}_5) = \text{Conv}_{1 \times 1}(\text{cat}(\mathcal{N}_5, \text{LAM}(\mathcal{N}_5))) \quad (18)$$

where “cat” represents the concatenation operation. The \mathcal{F}_1 operation adopts the LAM to help the model choose better normal features and processes one feature cube. In contrast, the

\mathcal{F}_2 operation fuses two feature cubes from the corresponding encoder and decoder parts. Taking \mathcal{N}'_5 and \mathcal{N}'_4 as an example, the \mathcal{F}_2 operation can be expressed as shown in Eq. (19):

$$\mathcal{F}_2(\mathcal{N}'_4, \mathcal{N}'_5) = \text{Conv}_{1 \times 1}(\text{cat}(\mathcal{N}'_4, \text{Up}(\mathcal{N}'_5))) \quad (19)$$

\mathcal{N}'_5 is first upsampled to the same spatial size as \mathcal{N}'_4 , and then fused with \mathcal{N}'_4 using a similar approach to Eq. (18).

$P(\mathcal{N} | \mathcal{D})$ is naturally instantiated as the layer connection because the cascaded deep model itself is a kind of graph model. The edge corresponding to $P(\mathcal{N} | \mathcal{D})$ converts \mathcal{D} into \mathcal{N} . According to the reformulated workflow, $P(\mathcal{D} | \mathcal{N})$ is exactly the resulting anomaly map. To compute $P(\mathcal{D} | \mathcal{N})$, the \mathcal{F}_2 operation is first used to fuse the representative \mathcal{N} (i.e., \mathcal{N}'_1) with \mathcal{D} to obtain T (as shown in Fig. 3(b)), and then the output head considers \mathcal{N} and \mathcal{D} simultaneously to output the final anomaly map. In fact, the output head implicitly performs the Bayes transformation.

3.2.3 Optimization for Conditional Probabilistic Ranking

In the reformulated detection workflow, Eqs. (14) and (5) give the learning objective (i.e., the conditional probabilistic ranking of $P(\mathcal{D} | \mathcal{N})$), where Eq. (14) is the expanded form of Eq. (5). In this part, Eqs. (14) and (5) are instantiated as the feature-level and pixel-level optimizations, respectively.

Feature-level optimization. Feature-level optimization is conducted on the feature cube T according to Eq. (14). Each component in this part is extracted with the simulated label (H_{al} or S_{al}) from T . Equation (14) focuses on the compactness ranking for the different components. The normalized compactness sum of $(\mathcal{D}_b, \mathcal{D}_l)$ and $(\mathcal{D}_b, \mathcal{D}_l, \mathcal{N}_b, \mathcal{N}_l)$ is expected to exceed the compactness sum of (\mathcal{D}_a) and $(\mathcal{D}_a, \mathcal{N}_b, \mathcal{N}_l)$.

We instantiate the compactness measure M_3 by constructing the enclosing hypersphere with center \mathbf{c} and radius R around the descriptors (as shown in Fig. 3(c)), inspired by [35], [60]. Maximizing M_3 aims to minimize R as much as possible while keeping the hypersphere wrapping most of the descriptors. Taking $M_3(\mathcal{D}_a, \mathcal{N}_b, \mathcal{N}_l)$ as an example, \mathbf{c} can be computed as shown in Eq. (20), and M_3 can be computed as shown in Eq. (21). d represents the single descriptor and parameter β controls the tradeoff. $M_3(\mathcal{D}_b, \mathcal{D}_l, \mathcal{N}_b, \mathcal{N}_l)$ can be computed in a similar way.

$$\mathbf{c} = \text{mean}(d_i), d_i \in (\mathcal{D}_a, \mathcal{N}_b, \mathcal{N}_l) \quad (20)$$

$$M_3(\mathcal{D}_a, \mathcal{N}_b, \mathcal{N}_l) = -(R^2 + \beta \text{mean}(\max\{\|d_i - \mathbf{c}\|^2 - R^2, 0\}) | d_i \in (\mathcal{D}_a, \mathcal{N}_b, \mathcal{N}_l)) \quad (21)$$

Based on the simple fact that the M_1 compactness and the corresponding M_3 compactness are positively correlated, Eq. (14) can be simplified to Eq. (22). To prevent negative loss and remove the constant terms, the final feature-level optimization objective \mathcal{L}_f can be written as shown in Eq. (23).

$$\begin{aligned} \max & \left(\frac{1}{Z_1} \exp(M_3(\mathcal{D}_b, \mathcal{D}_l, \mathcal{N}_b, \mathcal{N}_l)) \right. \\ & \left. - \frac{1}{Z_2} \exp(M_3(\mathcal{D}_a, \mathcal{N}_b, \mathcal{N}_l)) \right) \quad (22) \\ \mathcal{L}_f = \min & \left(-M_3(\mathcal{D}_b, \mathcal{D}_l, \mathcal{N}_b, \mathcal{N}_l) \right. \\ & \left. - \frac{1}{M_3(\mathcal{D}_a, \mathcal{N}_b, \mathcal{N}_l)} \right) \quad (23) \end{aligned}$$

Pixel-level optimization. Pixel-level optimization is conducted on the output $P(\mathcal{D} | \mathcal{N})$ according to Eq. (5). Equation (5) transfers the binary classification problem into a ranking problem, which expects $P(\mathcal{D}_b | \mathcal{N})$ and $P(\mathcal{D}_l | \mathcal{N})$ to be larger than $P(\mathcal{D}_a | \mathcal{N})$. In view of the ranking optimization always being evaluated with the AUC metric, we derived the objective starting from the AUC definition. Given a changing false alarm rate η , the AUC can be written in the integral form, as shown in Eq. (24) [61], where TPR represents the true positive rate and FPR represents the false positive rate. $\text{TPR} @ \text{FPR}_\eta(P)$ is defined as shown in Eq. (25) ($P(\mathcal{D} | \mathcal{N})$ is abbreviated to P unless otherwise specified).

$$\text{AUC} = \int_0^1 \text{TPR} @ \text{FPR}_\eta(P) d\eta \quad (24)$$

$$\text{TPR} @ \text{FPR}_\eta(P) = \max \text{TPR}(P) \quad \text{s.t.} \quad \text{FPR}(P) < \eta \quad (25)$$

TPR and FPR need to be computed with the additional segmentation threshold th , where th converts the score map P into a binary map P_{th} . We let $|\mathcal{D}_a|$ and $|\mathcal{D}_n|$ be the number of anomaly and normal pixel descriptors, respectively. The TPR and FPR can then be written explicitly, as shown in Eqs. (26) and (27):

$$\text{TPR} = \frac{tp(P_{th})}{tp(P_{th}) + fn(P_{th})} = \frac{tp(P_{th})}{|\mathcal{D}_a|} \quad (26)$$

$$\text{FPR} = \frac{fp(P_{th})}{|\mathcal{D}_a|} \quad (27)$$

where tp , fp , and fn are the true positives, false positives, and false negatives. They can be defined with the indicator function I (as shown in Eqs. (28) and (29) for tp and fp).

$$tp(P_{th}) = \sum_{d_i \in \mathcal{D}_n} I(d_i \geq th) \quad (28)$$

$$fp(P_{th}) = \sum_{d_i \in \mathcal{D}_a} I(d_i < th) \quad (29)$$

The difficulty of optimizing Eqs. (28) and (29) lies in the fact that function I is not differentiable, and is not suitable for the common backward optimization. Some related studies introduced sigmoid loss or the hinge loss function to make I differentiable [61], [62]. However, the sigmoid loss needs another hyperparameter to control the smoothness, and the large margin setting of hinge loss is difficult to set. To this end, we adapted the robust cross-entropy loss (i.e., \mathcal{L}_{ce}) to redefine tp and fp , as shown in Eqs. (30) - (32):

$$tp_{ce}(P_{th}) = 1 - \sum_{d_i \in \mathcal{D}_n} \mathcal{L}_{ce}(d_i, th) \leq tp(P_{th}) \quad (30)$$

$$fp_{ce}(P_{th}) = \sum_{d_i \in \mathcal{D}_a} \mathcal{L}_{ce}(d_i, th) \geq fp(P_{th}) \quad (31)$$

$$\mathcal{L}_{ce}(d_i, th) = \begin{cases} -\log(P_{d_i}) & \text{if } d_i \in \mathcal{D}_n \text{ and } P_{d_i} > th \\ \frac{\log(P_{d_i})}{\log th} & \text{if } d_i \in \mathcal{D}_n \text{ and } P_{d_i} < th \\ -\log(1 - P_{d_i}) & \text{if } d_i \in \mathcal{D}_a \text{ and } P_{d_i} < th \\ \frac{\log(1 - P_{d_i})}{\log th} & \text{if } d_i \in \mathcal{D}_a \text{ and } P_{d_i} > th \end{cases} \quad (32)$$

Equation (32) ensures that the inequality in Eqs. (30) and (31) holds, where $tp_{ce}(P_{th})$ is the lower bound of $tp(P_{th})$ and $fp_{ce}(P_{th})$ is the upper bound of $fp(P_{th})$. th replaces 0.5 as the threshold that varies with η . We divide the original cross-entropy loss by $\log th$ to make $\mathcal{L}_{ce}(d_i, th)$ larger than 1.0 and the inequality holds. The inequality relationship in Eq. (29) implies that Eq. (25) can be transformed into Eq. (33):

$$TPR @ FPR_{\eta}(P) = \min(1 - tp_{ce}(P_{th})) \text{ s.t. } \frac{fp_{ce}(P_{th})}{|\mathcal{D}_a|} < \eta \quad (33)$$

Then, using Lagrange multiplier theory, Eq. (33) can be rewritten as Eq. (34) with the Lagrange multiplier λ :

$$\min_{P_{th}} \max_{\lambda} (1 - tp_{ce}(P_{th})) + \lambda (fp_{ce}(P_{th}) - \eta |\mathcal{D}_a|) \quad (34)$$

Finally, we substitute Eq. (34) into Eq. (23) and approximate the integral with a discrete sum over the FPR anchor values. We suppose that k anchors exist in the range $[0, 1]$, with each anchor corresponding to the false alarm rate η_t , threshold th_t , and multiplier λ_t . $\lambda_t = \eta_t - \eta_{t-1}$ for $\forall t = 1 \dots k$. Equation (35) then gives the final pixel-level optimization objective \mathcal{L}_p :

$$\mathcal{L}_p = \min_{P_{th}, th_1, \dots, th_k} \max_{\lambda_1, \dots, \lambda_k} \sum_{t=1}^k \left(\Delta_t (1 - tp_{ce}(P_{th})) + \lambda_t (fp_{ce}(P_{th_t}) - \eta_t |\mathcal{D}_a|) \right) \quad (35)$$

\mathcal{L}_f and \mathcal{L}_p work together to optimize the deviation relationship learning in feature-level and pixel-level respectively. The final optimization objective is their weighted sum in Eq. (36), where w controls the balance.

$$\mathcal{L} = w\mathcal{L}_f + \mathcal{L}_p \quad (36)$$

4. EXPERIMENTAL RESULTS

4.1 Experimental Settings

In this section, we describe how the proposed UniADRS model was validated in five modalities, i.e., hyperspectral, visible light, SAR, infrared, and low-light, to show its cross-modal ability. Each modality had changing scenes to show the cross-scene ability. We first describe the comparative experiments conducted with other non-unified models, which were trained separately on each scene. Then, the ablation study results and the model efficiency are also discussed.

4.1.1 Constructed Multi-Modal Dataset

We built a multi-modal dataset for the ADRS task, with hyperspectral, visible light, SAR, infrared, and low-light modalities (as detailed in Table 1). The images in the dataset cover various scenes, sensor types, and resolutions. The 82 hyperspectral scenes were collected from the Cri dataset [50] and the two large-scale unmanned aerial vehicle (UAV)-borne datasets of WHU-Hi-Park and WHU-Hi-Station [32]. For the

TABLE 1
The Detailed Information of Constructed Multi-modal Dataset for the ADRS Task

Modality	Source	Spatial resolution	Image size	Scene number	Anomalies
Hyperspectral	Nuance Cri; Nano-Hyperspec	4–8 cm/pixel	400×400; 200×200	82	Plastic plane, metal object, etc. [32]
Visible light	Google Earth	0.5–2 m/pixel	1044×915	100	Military camouflage [42], aircraft [10]
SAR	Gaofen-3; Sentinel-1	3–10 m/pixel	256×256	100	Various ships [8]
Infrared	\	\	173×98; 407×305	100	Car, dim lamp, etc. [39]
Low-light	Indigo NV-400-M	\	2048×2048	100	Toy car, plane, tank, etc.

low-light modality, we first captured 50 scenes at night and then doubled this by data augmentation to make the overall size balanced. The multi-modal dataset will be made publicly available.

4.1.2 Comparison Methods and Evaluation Metrics

Due to the property of the high spectral resolution, the hyperspectral modality has many unique models and was considered separately from the other modalities.

The comparative models for the hyperspectral modality were the global RX detector (GRX) [13], the abundance- and dictionary-based low-rank decomposition (ADLR) detector [63], the collaborative representation based (CRD) detector [20], the spectral constraint autoencoder (SC_AAE) detector [25], the deep low-rank prior based detector (DeepLR) [32], and the TDD method [29]. The comparison methods cover the three categories of statistical-based, representation-based, and deep learning based methods.

The comparative models for the remaining four modalities were GRX [31], a convolutional autoencoder (CAE) [64], a variational autoencoder (VAE) [65], the saliency-based method proposed by Cai *et al* [24] and an adversarial autoencoder (AAE) [21]. The implementation of these methods was adapted from the related ADRS studies [21], [24], [31], [65]. Besides, we also compared UniADRS with the state-of-art industrial anomaly detection model UniAD [37]. To adapt the UniAD for the small objects in ADRS task, the input size is increased from 224 to 1024. The remaining settings are kept same as [37].

In this paper, the detection performance is evaluated with multi-parameter 3D receiver operating characteristic (3D ROC) curves [66]. Compared to 2D ROC curves, the threshold dimension is additionally considered and can provide more comprehensive information. The used metrics are the widely used $AUC_{(D,F)}$, the target detectability AUC_{TD} , the background suppressibility AUC_{BS} , and the overall detection probability AUC_{ODP} . Each metric value is positively correlated with the detection performance.

4.1.3 Implementation Details

We set the hyperparameters of the comparative hyperspectral

models following [29]. The CAE architecture was Unet with a ResNet50 backbone. For the SAR modality, speckle removal was conducted before applying the AAE method, following [21]. Each input image was resized to 224×224 for UniADRS and the comparative methods at the training stage. When simulating the spectral anomalies, we controlled the O_a area in the ratio range $[0.0064, 0.0225]$ and O_l in the range $[0.0225, 0.5]$. Similarly, we controlled the O_a area in the ratio range $[0.02, 0.06]$ and O_l in the range $[0.06, 0.5]$ for the simulated spatial anomalies. At most, two O_a and two O_l objects were generated for each simulated anomaly sample. The feature-level optimization loss and the pixel-level loss were added at a ratio of 0.1:1. The UniADRS was optimized with the Adam optimizer (learning rate 0.01, weight decay $1e-5$) over 100 epochs. w was set 0.5. The spectral anomaly sample and the spatial anomaly sample were randomly selected for each iteration. The CPU was an Intel(R) Xeon(R) CPU E5-2690 v4 @ 2.60 GHz with 62 GB memory, and the GPU was a Tesla P100-PCIE with 16 GB of memory.

4.2 Comparison Results

Results for the hyperspectral modality. Table 2 lists the quantitative results. Although UniADRS inferred the test images directly without retraining, it is the only model that achieves an $AUC_{(D,F)}$ metric score of higher than 0.97 and an AUC_{ODP} metric score of higher than 1.35 on all three datasets, demonstrating great transferability. Considering the 82 scenes together, UniADRS obtains the optimal values in three metrics. Although the TDD model shows satisfactory transferability on the Cri dataset, the metric scores drop dramatically on the UAV-borne WHU-Hi Park and Station datasets ($AUC_{(D,F)}$ 0.67 and 0.71, respectively). This may have been caused by the lack of consideration for the large normal objects at the training stage, which are common in UAV images due to the high spatial resolution.

Fig. 6 visualizes the anomaly maps for two example scenes. The high spatial resolution brings more details as well as more

TABLE 2
Quantitative Results for the Hyperspectral Modality, Dozens of Scenes in WHU-Hi Park and WHU-Hi Station are Evaluated Together

Method	$AUC_{(D,F)}$	AUC_{TD}	AUC_{BS}	AUC_{ODP}	$AUC_{(D,F)}$	AUC_{TD}	AUC_{BS}	AUC_{ODP}
Scene	Cri (1 scene)				WHU-Hi Park (27 scenes)			
GRX	0.9678	1.1932	0.8782	1.1036	0.9379	1.3091	0.8099	1.2432
ADLR	0.9579	1.9253	0.3159	1.2833	0.8234	1.0784	0.7995	1.2311
CRD	0.9186	1.1350	0.8738	1.0902	0.9095	1.1046	0.8514	1.1370
SC_AAE	0.8849	1.1355	0.8608	1.1114	0.9579	1.1798	0.9509	1.2149
DeepLR	0.9815	1.2465	0.9687	1.2337	0.9736	1.1837	0.9607	1.1972
TDD	0.9915	1.6298	0.8793	1.5176	0.6712	0.7391	0.0464	0.7855
UniADRS	0.9970	1.6755	0.9472	1.6257	0.9748	1.4181	0.9331	1.3764
	WHU-Hi Station (54 scenes)				Average			
GRX	0.8988	1.1441	0.8163	1.1628	0.9348	1.1304	0.8547	1.1146
ADLR	0.9260	1.3566	0.8650	1.3696	0.9024	1.0861	0.8293	1.1414
CRD	0.9722	0.9763	0.9719	1.0038	0.9334	0.9968	0.9109	1.0168
SC_AAE	0.9708	1.0455	0.9701	1.0740	0.9379	1.0611	0.9596	1.0823
DeepLR	0.9853	1.1169	0.9825	1.1288	0.9801	1.0914	0.9723	1.0999
TDD	0.7190	0.2051	0.5940	0.7991	0.7939	0.5385	0.4372	0.7519
UniADRS	0.9860	1.3896	0.9512	1.3548	0.9859	1.2608	0.9530	1.2353

disturbance. Compared to the Cri dataset, the WHU-Hi-Station dataset has more background categories, including roads, trees, and large buildings. Predictably, the statistical-based and representation-based methods show a high level of false alarms, and the large buildings are wrongly considered as anomalies. Although the deep learning based methods show a better background suppression ability, the response values for the anomaly pixels are also low, making the manual interpretation difficult. In contrast, UniADRS has both a low false alarm rate and better discriminability, which are advantageous for the anomaly detection.

Results for the visible light modality. The quantitative results are listed in Table 3(a). The proposed UniADRS model achieves the best performance under the $AUC_{(D,F)}$ and AUC_{BS} metrics, even without retraining on the visible light images. UniADRS and UniAD are the only two models with an $AUC_{(D,F)}$ score of higher than 0.80. Although the AUC_{TD} score of UniADRS is lower than that of GRX, this could be improved with a simple post-processing of image stretching.

Fig. 7 visualizes the anomaly maps for the visible light modality. The anomaly (i.e., the camouflage net) in the first scene is very inconspicuous and many detectors fail to find it. The second scene comes from the Russo-Ukrainian War, where a Russia tank is hiding, which a Ukrainian UAV attempted to blow up. Many of the methods correctly locate the anomalies in this scene, but with an incomplete shape. Since UniADRS has seen millions of high-resolution objects, its result has the most complete anomaly shape. Although GRX also successfully locates all of the anomalies, the high false alarm rate brings serious disturbance. Compared to the other methods, UniADRS achieves the best tradeoff between correct detection and false alarms.

Results for the SAR modality. UniADRS shows a similar performance ranking to the visible light modality in Table 3(b), where all the methods have higher $AUC_{(D,F)}$ values for the SAR modality. On the one hand, the detection is relatively easy for

most of the SAR scenes, because the anomalies (i.e., ships) lie in a homogeneous sea background. On the other hand, the scenes with harbor or building background are difficult to handle due to the well-known speckle noise problem. This can be seen in the qualitative results in Fig. 8, where the background contains both harbors and buildings. The statistical method of GRX fails to process the speckle noise and the obtained anomaly map is full of salt-and-pepper noise. Although the reconstruction-based methods alleviate the noise impact by introducing spatial information, some noisy pixels still exist. Since the tested SAR image only has one channel, CAE tends to reconstruct both the background and anomalies, which is exactly the problem of the reconstruction-based methods. The method proposed by Cai *et al.* obtains an $AUC_{(D,F)}$ value of 0.86 but performs worse in the two exemplified scenes because the harbors and buildings make the saliency detector lose focus easily, which can be avoided with the complete sea background. UniAD has achieved high $AUC_{(D,F)}$ (0.9102) but the anomaly maps are difficult to distinguish and require some post-processing (e.g. stretching). It can be seen that the anomalies always have higher pixel values, so why not set a threshold directly? This can be attributed to two points. Firstly, there are also normal buildings with high pixel values, such as the top right corner of the first scene. Secondly, spatial information is necessary to tackle the speckle noise. Overall, the proposed UniADRS model can process the speckle noise of the SAR modality well and detect the anomalies without retraining.

Results for the infrared modality. UniADRS achieves the highest $AUC_{(D,F)}$ score of 0.94 in Table 3(c), which already surpasses the supervised result in [39], even when inferred directly. Exemplified results on two scenes with different backgrounds are shown in Fig. 9. The anomalies always show an unusual thermal pattern, regardless of the light, which plays an important role in nighttime detection. The first scene has a large thermal area and brings serious disturbance to the detection of GRX, VAE, AAE and UniAD. Due to the explicit modeling of large normal objects, UniADRS can recognize the

TABLE 3
Quantitative Results for the Visible Light, SAR, Infrared, and Low-Light Modalities

Method	$AUC_{(D,F)}$	AUC_{TD}	AUC_{BS}	AUC_{ODP}	$AUC_{(D,F)}$	AUC_{TD}	AUC_{BS}	AUC_{ODP}
	(a) Visible light modality				(b) SAR modality			
GRX	0.7292	1.1506	0.5210	0.9425	0.8938	1.5250	0.7931	1.4243
CAE	0.7970	0.8771	0.7715	0.8516	0.8281	0.9118	0.8210	0.9047
VAE	0.6891	1.0159	0.5552	0.8819	0.8816	1.3315	0.8495	1.2995
Cai <i>et al.</i>	0.7567	0.9205	0.7005	0.8644	0.8610	1.0612	0.8347	1.0349
AAE	0.7101	0.9260	0.6375	0.8534	0.8831	0.9699	0.8757	0.9626
UniAD	0.8546	1.0217	0.7931	0.9603	0.9102	1.0678	0.8329	0.9905
UniADRS	0.8948	0.9207	0.8901	0.9160	0.9595	0.9959	0.9549	0.9913
	(c) Infrared modality				(d) Low-light modality			
GRX	0.6814	1.0899	0.4543	0.8629	0.6684	1.0900	0.4647	0.8863
CAE	0.8291	0.9297	0.8180	0.9187	0.6246	0.6620	0.6005	0.6380
VAE	0.7301	1.2339	0.4902	0.9941	0.5703	0.7299	0.4899	0.6495
Cai <i>et al.</i>	0.8853	1.2242	0.8415	1.1805	0.8248	0.9900	0.8049	0.9701
AAE	0.7557	1.0686	0.6598	0.9727	0.6694	0.8224	0.6196	0.7726
UniAD	0.8348	0.9145	0.8054	0.8850	0.7716	0.8563	0.7343	0.8191
UniADRS	0.9437	0.9820	0.9394	0.9778	0.8336	0.8558	0.8291	0.8513

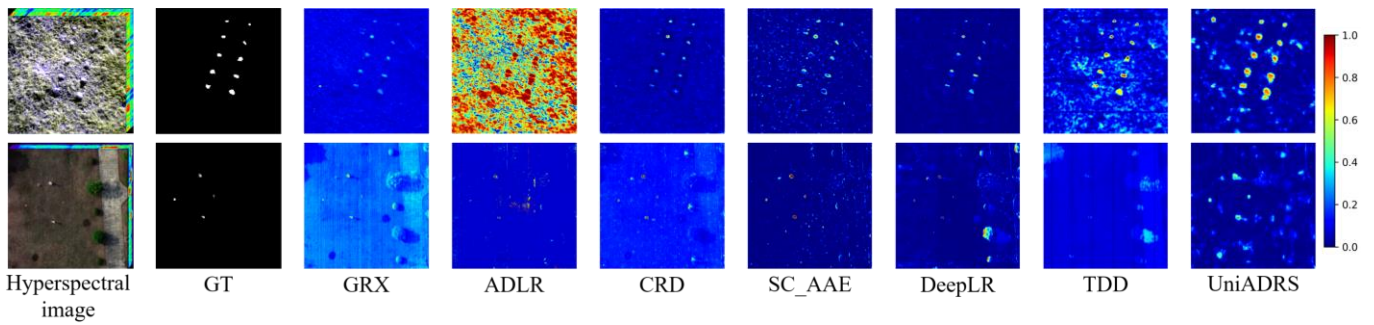


Fig. 6. Typical anomaly detection results for the hyperspectral modality, where the anomalies include rocks (first row), fabric camouflage objects (second row) and metal objects (second row).

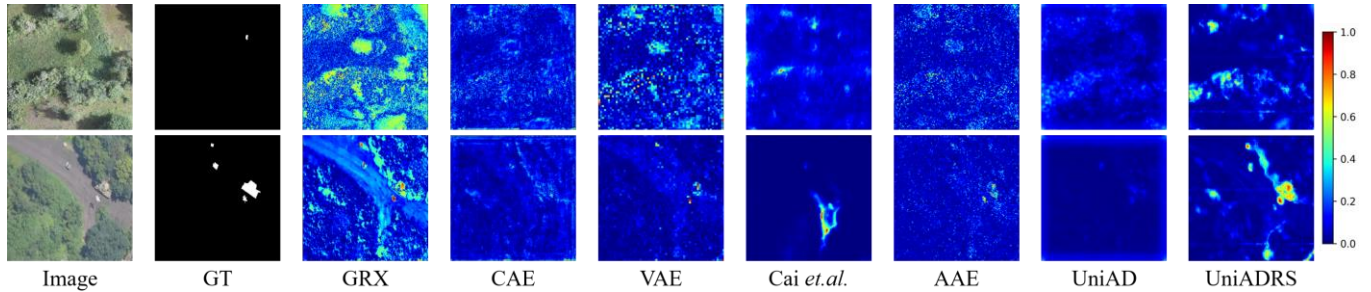


Fig. 7. Typical anomaly detection results for the visible light modality, where the anomalies include the camouflage net (first row), a tank and a drone (second row).

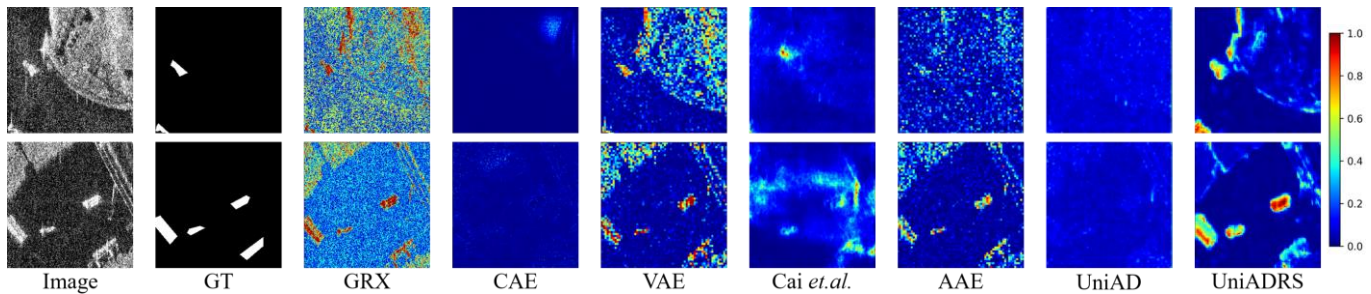


Fig. 8. Typical anomaly detection results for the SAR modality, where the anomalies include various ships.

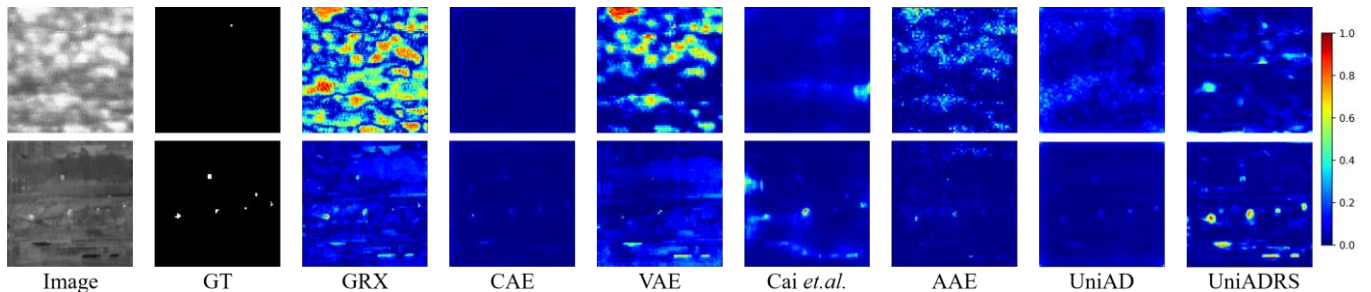


Fig. 9. Typical anomaly detection results for the infrared modality, where the anomalies include the plane (first row) and peoples (second row).

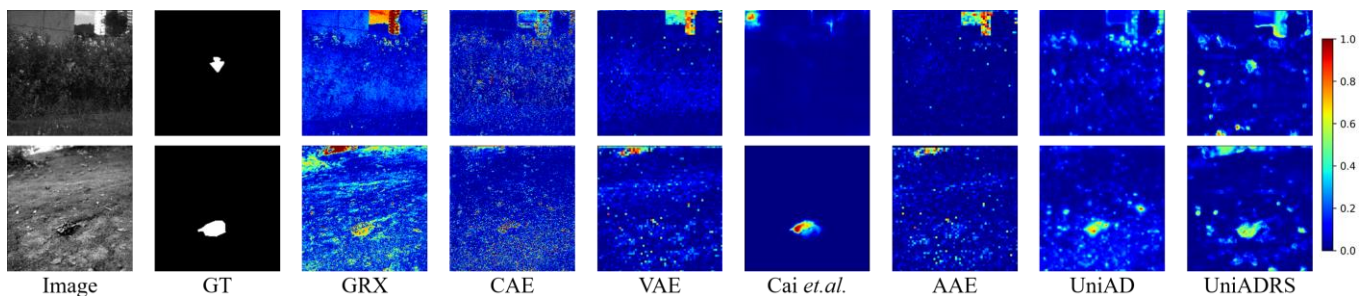


Fig. 10. Typical anomaly detection results for the low-light modality, where the anomalies include a toy plane (first row) a toy tank (second row).

anomalies correctly. Although CAE and VAE find the anomalies successfully, many background pixels have the same level of response as the anomalies, increasing the burden of the downstream processing. The anomaly maps of UniADRS can be easily discriminated, with fewer disturbances.

Results for the low-light modality. The captured low-light dataset has lower contrast than the remaining modalities (as shown in Table 3(d) and Fig. 10), making the detection more challenging. UniADRS and the method of Cai *et al.* both achieve $AUC_{(D,F)}$ values of higher than 0.80, demonstrating that the saliency-based approach is more suitable for the single-object scenes than the scenes with many anomalies (e.g., the visible light modality). It can be observed that UniADRS has the best background suppression ability (i.e., the highest AUC_{BS} score) in the four modalities with spatial anomalies. This can be attributed to the explicit modeling of the background and the large objects in the reformulated workflow and the instantiation process. Fig. 10 shows two scenes where the anomalies have a low contrast with the background. Differing from its performance in the prior modalities, GRX fails to detect the anomalies in the first two scenes, which also have many noisy pixels as well. The original anomaly maps of CAE all have low response values, and thus we applied the 2% linear stretching to the results. The methods of Cai *et al.* and UniAD have successfully identified the anomaly in second scene but failed for the first scene. In contrast, UniADRS can detect the both anomalies in the low-contrast scenes with discriminative boundaries and high confidence.

4.3 Ablation Study Results

To validate the effectiveness of each ingredient, ablation experiments were conducted for the sample simulation and the model optimization.

4.3.1 Sample Simulation

In the proposed UniADRS model, we simulate both the spectral anomalies and spatial anomalies, where the background, large normal objects, and anomalies are explicitly

modeled. With the simulated samples, UniADRS can be trained following the one-step paradigm. From the prior compared results, the explicit model for large normal objects O_l plays an important role in decreasing the false alarms. Thus, we conducted the ablation experiments from two aspects: whether to simulate the large normal objects and whether to simulate both kinds of anomalies. The related results are shown in Table 4. Comparing row 1 with row 2, and row 3 with row 4, it is clear that the O_l simulation can bring a stable gain in most modalities and scenes. Especially for the large-scale hyperspectral datasets—WHU-Hi Park and WHU-Hi Station—there is an increase of around 10 points in the $AUC_{(D,F)}$ metric. A similar significant increase can be observed for the visible light modality. For the modalities with a lot of simple scenes, such as the infrared and low-light modalities, the increase is lower. We deduce that the gain obtained from the O_l simulation is positively correlated with the scene complexity. For the simulation of both spectral anomalies and spatial anomalies, the spatial anomaly simulation can result in a more robust performance in most modalities, regardless of the O_l simulation. Even for the hyperspectral modality, training the spatial stem only can obtain better results than training the spectral stem only. Despite this, the $AUC_{(D,F)}$ metric is only 0.91 on the large-scale WHU-Hi Station dataset with either the spatial or spectral stem only. The reason for this can be easily deduced. For the UAV scene, the pixels have both a high spatial resolution and high spectral resolution, making the spatial features and spectral features both important for accurate detection. Thus, training the spatial and spectral stems together increases the $AUC_{(D,F)}$ from 0.91 to 0.98 on the WHU-Hi Station dataset, and a stable increase is obtained for most of the other modalities. Overall, the O_l simulation benefits the detector on complex scenes, and the inclusion of both the spatial and spectral stems helps the detector to better fuse the spatial and spectral features.

TABLE 4
Ablation Results for the Designed Anomaly Sample Simulation Strategy

Spectral stem	Spatial stem	O_l Simulation	Hyperspectral	Visible light	SAR	Infrared	Low-light	Average
			$AUC_{(D,F)}$	$AUC_{(D,F)}$	$AUC_{(D,F)}$	$AUC_{(D,F)}$	$AUC_{(D,F)}$	$AUC_{(D,F)}$
√	×	×	0.8668	0.7390	0.8674	0.7683	0.6988	0.8106
√	×	√	0.9377	0.8285	0.8038	0.8012	0.7375	0.8549
×	√	×	0.9256	0.7916	0.9211	0.8168	0.8136	0.8743
×	√	√	0.9538	0.8597	0.9667	0.8703	0.7815	0.9056
√	√	√	0.9859	0.8948	0.9595	0.9437	0.8336	0.9416

TABLE 5
Ablation Results for the Designed Model Optimization Loss

Optimization loss	Hyperspectral	Visible light	SAR	Infrared	Low-light	Average
	$AUC_{(D,F)}$	$AUC_{(D,F)}$	$AUC_{(D,F)}$	$AUC_{(D,F)}$	$AUC_{(D,F)}$	$AUC_{(D,F)}$
Cross-entropy loss	0.9409	0.8937	0.9634	0.9296	0.8213	0.9187
Dice loss	0.9281	0.8720	0.8786	0.8531	0.7600	0.8783
Pixel-level optimization	0.9641	0.8851	0.9506	0.9337	0.8434	0.9293
Pixel-level and feature level	0.9859	0.8948	0.9595	0.9437	0.8336	0.9416

TABLE 6

Efficiency Comparison for the Hyperspectral Modality. The Last Row Shows the Speed Increase and the Consequent Drop in $AUC_{(D,F)}$ of UniADRS by Increasing the Inferring Patch Size

Method	Cri	WHU-Hi Park	WHU-Hi Station
GRX	3.73s	51.91s	71.96s
ADLR	1258.50s	25405.03s	34227.51s
CRD	1024.84s	37427.60s	37181.45s
SC_AAE	128.91s	9944.33s	21728.03s
DeepLR	31.49s	10187.13s	13714.35s
TDD	4.21s	94.51s	166.38s
UniADRS	5.14s	59.13s	121.98s
UniADRS	0.55s ($\downarrow 0.1$)	12.46s ($\downarrow 2$)	10.39s ($\downarrow 5$)

TABLE 7

Efficiency Comparison for the Visible Light, SAR, Infrared, and Low-Light Modalities. The Last Row Shows the Speed Increase and the Consequent Drop in $AUC_{(D,F)}$ of UniADRS by Inferring the Whole Image Directly

Method	Visible light modality	SAR modality	Infrared modality	Low-light modality
GRX	37.52s	56.67s	41.08s	123.12s
CAE	172.64s	162.23s	646.43s	129.30s
VAE	113.77s	227.38s	71.60s	185.98s
Cai <i>et al.</i>	268.73s	371.39s	1236.66s	1452.26s
AAE	160.63s	153.19s	659.41s	1202.76s
UniAD	7440.16s	3120.53s	5760.88s	6324.86s
UniADRS	83.68s	107.69s	64.64s	61.75s
UniADRS	10.39s ($\downarrow 5$)	10.07s ($\downarrow 1$)	11.97s ($\downarrow 1$)	34.20s ($\downarrow 2$)

4.3.2 Model Optimization

Pixel-level and feature-level optimization are proposed, according to the learning target in the constructed undirected bilayer graph. To show the superiority of this approach, we compared it with classical cross-entropy (CE) loss and dice loss, and we also validated the feature-level optimization separately. CE loss and dice loss can be considered as surrogates, while the proposed optimization approach is specially designed for the ADRS task. Table 5 lists the related results. Not surprisingly, all four settings can optimize UniADRS successfully with the designed sample simulation strategy. The results of dice loss are the worst, relatively, with many metric values lower than 0.90. Although dice loss is widely used in the segmentation task, it may be better to evaluate the performance with the intersection over union (IoU) rather than $AUC_{(D,F)}$. With the proposed pixel-level optimization only, a slightly better performance can be observed than with CE loss. Especially for the large-scale WHU-Hi Park and WHU-Hi Station datasets, this approach surpasses the CE loss by around 3 and 5 points, respectively. For the remaining modalities and scenes, the performance is similar. After adding the feature-level optimization, a stable promotion can be obtained, except for the low-light modality (1-point decrease). Note that using feature-level optimization only is not sufficient because the final detection head would have no gradient to update. Using both the pixel-level and feature-level optimization, UniADRS obtains the highest $AUC_{(D,F)}$ score on most modalities and scenes.

4.4 Model Efficiency

One of the great advantages of the proposed UniADRS model is the elimination of training for each given scene. The prior experiments validated the model effectiveness, where UniADRS was superior to the existing methods designed for a certain modality. In this section, the efficiency of UniADRS is further investigated by computing the model processing time for each modality and scene. Note that the deep learning based methods were all tested on a GPU device, and the statistical-based and representation-based methods were tested on a CPU. There is indeed some unfairness here. Despite this, the resulting time increase also reflects the limitation of CPU in parallel computing.

Table 6 lists the recorded processing times for the hyperspectral modality. The comparative methods are well-designed to improve the accuracy, but the time cost also increases greatly. The classical GRX method is very efficient and has the ability to process the large-scale WHU-Hi datasets in around one minute. In contrast, the representation-based and deep learning based methods need a longer time, of two or three orders of magnitude, especially for the traditional deep learning based methods. For example, the current state-of-the-art model of DeepLR needs around 3 and 4 hours for the WHU-Hi Park and WHU-Hi Station datasets, respectively. Although TDD can deal with the WHU-Hi scenes in less than 2 min, the accuracy is not satisfactory, as shown in Table 2. With the highest accuracy performance, the proposed UniADRS model can process the scenes faster than the representation-based and deep learning based methods, and the time is closer to that of GRX. If we increase the inference patch size further, the processing time can be decreased to less than 1 s for the Cri dataset, and around 10 s for the WHU-Hi datasets. The consequent accuracy decrease can be seen in Table 6. The obtained results fully prove the real-time performance of UniADRS, and its ability to process large-scale hyperspectral scenes.

Table 7 lists the recorded processing times for the remaining four modalities without spectral information. Thanks to the GPU acceleration and low band number, the training time of the deep learning based methods is not as long as for the hyperspectral modality, and most are around several hundred seconds. Since UniAD needs around 100 epochs to converge, the resulting times are the longest in all the four modalities. The main time consumption of UniADRS comes from the overlapping inference, to make the anomaly ratio consistent with the training setting. If we reduce the accuracy pursuit slightly and infer the whole image directly (rather than patches), UniADRS can process the four modalities in tens of seconds. The acceptable accuracy decrease is given in Table 7.

5. CONCLUSION

In this study, we designed a unified anomaly detector for different remote sensing modalities and scenes by reformulating the task as a bilayer undirected graph. The deviation of the anomalies and background is the focus, rather than the certain background distribution of the traditional methods. Comparative experiments with five modalities

confirmed the superiority of UniADRS, even without any fine-tuning. The efficiency test in Section 4.4 demonstrated that UniADRS can decrease the processing time by two or three orders of magnitude. Overall, UniADRS can achieve an accurate and fast anomaly detection performance.

Although anomaly detection can extract the potential targets without prior knowledge, the detectors cannot distinguish between real anomalies and detections that are not of interest. The latter recognition step is necessary for practical application [34]. To date, few studies have tried to combine the tasks and construct a complete detection and recognition pipeline. UniADRS has unified the anomaly detection task for different modalities and scenes. However, unifying the anomaly detection and object recognition needs to be further considered.

ACKNOWLEDGMENT

This work was supported by National Key Research and Development Program of China under Grant No. 2022YFB3903404, in part by the National Natural Science Foundation of China under Grant No.42325105 and No.42101327, and in part by LIESMARS Special Research Funding.

REFERENCES

- [1] "Remote sensing: Rainforest shrinkage," *Nature*, vol. 454, no. 7201, p. 140, 2008.
- [2] S. Sun, J. Liu, X. Chen, W. Li, and H. Li, "Hyperspectral Anomaly Detection With Tensor Average Rank and Piecewise Smoothness Constraints," *IEEE Trans. Neural Networks Learn. Syst.*, pp. 1–14, 2022.
- [3] W. Qiao, "Research framework of remote sensing monitoring and real-time diagnosis of earth surface anomalies," *Acta Geod. Cartogr. Sin.*, vol. 51, no. 7, p. 1141, 2022.
- [4] J. M. Meyer, R. F. Kokaly, and E. Holley, "Hyperspectral remote sensing of white mica: A review of imaging and point-based spectrometer studies for mineral resources, with spectrometer design considerations," *Remote Sens. Environ.*, vol. 275, p. 113000, 2022.
- [5] Q. Xie, M. Zhou, Q. Zhao, Z. Xu, and D. Meng, "MHF-Net: An Interpretable Deep Network for Multispectral and Hyperspectral Image Fusion," *IEEE Trans. Pattern Anal. Mach. Intell.*, vol. 44, no. 3, pp. 1457–1473, 2022.
- [6] Y. Fu, T. Zhang, L. Wang, and H. Huang, "Coded Hyperspectral Image Reconstruction Using Deep External and Internal Learning," *IEEE Trans. Pattern Anal. Mach. Intell.*, vol. 44, no. 7, pp. 3404–3420, 2022.
- [7] M. Marom, R. M. Goldstein, E. B. Thornton, and L. Shemer, "Remote sensing of ocean wave spectra by interferometric synthetic aperture radar," *Nature*, vol. 345, no. 6278, pp. 793–795, 1990.
- [8] H. Guo, X. Yang, N. Wang, and X. Gao, "A CenterNet++ model for ship detection in SAR images," *Pattern Recognit.*, vol. 112, p. 107787, 2021.
- [9] Z. Zheng, Y. Zhong, J. Wang, A. Ma, and L. Zhang, "FarSeg++: Foreground-Aware Relation Network for Geospatial Object Segmentation in High Spatial Resolution Remote Sensing Imagery," *IEEE Trans. Pattern Anal. Mach. Intell.*, pp. 1–16, 2023.
- [10] Y. Long, Y. Gong, Z. Xiao, and Q. Liu, "Accurate object localization in remote sensing images based on convolutional neural networks," *IEEE Trans. Geosci. Remote Sens.*, vol. 55, no. 5, pp. 2486–2498, 2017.
- [11] K. Jiang *et al.*, "E2E-LIAD: End-to-end local invariant autoencoding density estimation model for anomaly target detection in hyperspectral image," *IEEE Trans. Cybern.*, 2021.
- [12] J. Liu, Z. Hou, W. Li, R. Tao, D. Orlando, and H. Li, "Multipixel Anomaly Detection With Unknown Patterns for Hyperspectral Imagery," *IEEE Trans. Neural Networks Learn. Syst.*, vol. 33, no. 10, pp. 5557–5567, 2022.
- [13] I. S. Reed and X. Yu, "Adaptive multiple-band CFAR detection of an optical pattern with unknown spectral distribution," *IEEE Trans. Acoust.*, vol. 38, no. 10, pp. 1760–1770, 1990.
- [14] H. Kwon and N. M. Nasrabadi, "Kernel RX-algorithm: a nonlinear anomaly detector for hyperspectral imagery," *IEEE Trans. Geosci. Remote Sens.*, vol. 43, no. 2, pp. 388–397, 2005.
- [15] S.-Y. Chen, Y. Wang, C.-C. Wu, C. Liu, and C.-I. Chang, "Real-time causal processing of anomaly detection for hyperspectral imagery," *IEEE Trans. Aerosp. Electron. Syst.*, vol. 50, no. 2, pp. 1511–1534, 2014.
- [16] S. Sun, J. Liu, and W. Li, "Spatial Invariant Tensor Self-Representation Model for Hyperspectral Anomaly Detection," *IEEE Trans. Cybern.*, 2023.
- [17] L. Li, W. Li, Q. Du, and R. Tao, "Low-Rank and Sparse Decomposition with Mixture of Gaussian for Hyperspectral Anomaly Detection," *IEEE Trans. Cybern.*, vol. 51, no. 9, pp. 4363–4372, 2021.
- [18] Q. Ling, Y. Guo, Z. Lin, and W. An, "A constrained sparse representation model for hyperspectral anomaly detection," *IEEE Trans. Geosci. Remote Sens.*, vol. 57, no. 4, pp. 2358–2371, 2018.
- [19] H. Su, Z. Wu, A.-X. Zhu, and Q. Du, "Low rank and collaborative representation for hyperspectral anomaly detection via robust dictionary construction," *ISPRS J. Photogramm. Remote Sens.*, vol. 169, pp. 195–211, 2020.
- [20] W. Li and Q. Du, "Collaborative representation for hyperspectral anomaly detection," *IEEE Trans. Geosci. Remote Sens.*, vol. 53, no. 3, pp. 1463–1474, 2014.
- [21] M. Muzeau, C. Ren, S. Angelliaume, M. Datcu, and J.-P. Ovarlez, "SAR Anomalies Detection based on Deep Learning," 2022.
- [22] W. Li, G. Wu, and Q. Du, "Transferred deep learning for anomaly detection in hyperspectral imagery," *IEEE Geosci. Remote Sens. Lett.*, vol. 14, no. 5, pp. 597–601, 2017.
- [23] H. Shin and K. Na, "Anomaly Detection using Elevation and Thermal Map for Security Robot," in *2020 International Conference on Information and Communication Technology Convergence (ICTC)*, 2020, pp. 1760–1762.
- [24] C. Lile and L. Yiqun, "Anomaly detection in thermal images using deep neural networks," in *2017 IEEE International conference on image processing (ICIP)*, 2017, pp. 2299–2303.
- [25] W. Xie, J. Lei, B. Liu, Y. Li, and X. Jia, "Spectral constraint adversarial autoencoders approach to feature representation in hyperspectral anomaly detection," *Neural Networks*, vol. 119, pp. 222–234, 2019.
- [26] X. Lu, W. Zhang, and J. Huang, "Exploiting embedding manifold of autoencoders for hyperspectral anomaly detection," *IEEE Trans. Geosci. Remote Sens.*, vol. 58, no. 3, pp. 1527–1537, 2019.
- [27] P. Sprechmann, A. M. Bronstein, and G. Sapiro, "Learning Efficient Sparse and Low Rank Models," *IEEE Trans. Pattern Anal. Mach. Intell.*, vol. 37, no. 9, pp. 1821–1833, 2015.
- [28] N. Huyen, X. Zhang, D. Quan, J. Chanussot, and L. Jiao, "AUD-Net: A Unified Deep Detector for Multiple Hyperspectral Image Anomaly Detection via Relation and Few-Shot Learning," *IEEE Trans. Neural Networks Learn. Syst.*, pp. 1–15, 2022.
- [29] J. Li, X. Wang, S. Wang, H. Zhao, L. Zhang, and Y. Zhong, "One-Step Detection Paradigm for Hyperspectral Anomaly Detection via Spectral Deviation Relationship Learning," *arXiv Prepr. arXiv2303.12342*, 2023.
- [30] I. Ahmed, T. Galoppo, X. Hu, and Y. Ding, "Graph Regularized Autoencoder and its Application in Unsupervised Anomaly Detection," *IEEE Trans. Pattern Anal. Mach. Intell.*, vol. 44, no. 8, pp. 4110–4124, 2022.
- [31] Y. Haitman, I. Berkovich, S. Havivi, S. Maman, D. G. Blumberg, and S. R. Rotman, "Machine Learning for Detecting Anomalies in SAR Data," in *2019 IEEE International Conference on Microwaves, Antennas, Communications and Electronic Systems (COMCAS)*, 2019, pp. 1–5.
- [32] S. Wang, X. Wang, L. Zhang, and Y. Zhong, "Deep Low-Rank Prior for Hyperspectral Anomaly Detection," *IEEE Trans. Geosci. Remote Sens.*, vol. 60, pp. 1–17, 2022.

- [33] C. Lin, S.-Y. Chen, C.-C. Chen, and C.-H. Tai, "Detecting newly grown tree leaves from unmanned-aerial-vehicle images using hyperspectral target detection techniques," *ISPRS J. Photogramm. Remote Sens.*, vol. 142, pp. 174–189, 2018.
- [34] S. Matteoli, M. Diani, and G. Corsini, "A tutorial overview of anomaly detection in hyperspectral images," *IEEE Aerosp. Electron. Syst. Mag.*, vol. 25, no. 7, pp. 5–28, 2010.
- [35] J. Li, X. Wang, H. Zhao, S. Wang, and Y. Zhong, "Anomaly Segmentation for High-Resolution Remote Sensing Images Based on Pixel Descriptors," *Proc. AAAI Conf. Artif. Intell.*, vol. 37, no. 4, pp. 4426–4434, 2023.
- [36] C.-I. Chang and S.-S. Chiang, "Anomaly detection and classification for hyperspectral imagery," *IEEE Trans. Geosci. Remote Sens.*, vol. 40, no. 6, pp. 1314–1325, 2002.
- [37] Z. You *et al.*, "A Unified Model for Multi-class Anomaly Detection," *Adv. Neural Inf. Process. Syst.*, vol. 35, pp. 4571–4584, Jun. 2022.
- [38] Y. Gong, X. Yu, Y. Ding, X. Peng, J. Zhao, and Z. Han, "Effective fusion factor in FPN for tiny object detection," in *Proceedings of the IEEE/CVF winter conference on applications of computer vision*, 2021, pp. 1160–1168.
- [39] H. Wang, L. Zhou, and L. Wang, "Miss detection vs. false alarm: Adversarial learning for small object segmentation in infrared images," in *Proceedings of the IEEE/CVF International Conference on Computer Vision*, 2019, pp. 8509–8518.
- [40] A. Schaum, "Joint subspace detection of hyperspectral targets," in *2004 IEEE Aerospace Conference Proceedings (IEEE Cat. No.04TH8720)*, 2004, vol. 3, pp. 1-1824 Vol.3.
- [41] T. P. Watson *et al.*, "Evaluation of aerial real-time RX anomaly detection," in *Algorithms, Technologies, and Applications for Multispectral and Hyperspectral Imaging XXIX*, 2023, vol. 12519, pp. 254–260.
- [42] S. Liu *et al.*, "Hyperspectral Real-time Online Processing Local Anomaly Detection via Multi-Line Multi-Band Progressing," *IEEE Trans. Geosci. Remote Sens.*, 2023.
- [43] M. J. Carlotto, "A cluster-based approach for detecting man-made objects and changes in imagery," *IEEE Trans. Geosci. Remote Sens.*, vol. 43, no. 2, pp. 374–387, 2005.
- [44] A. Banerjee, P. Burlina, and C. Diehl, "A support vector method for anomaly detection in hyperspectral imagery," *IEEE Trans. Geosci. Remote Sens.*, vol. 44, no. 8, pp. 2282–2291, 2006.
- [45] P. K. Pokala, R. V. Hemadri, and C. S. Seelamantula, "Iteratively Reweighted Minimax-Concave Penalty Minimization for Accurate Low-rank Plus Sparse Matrix Decomposition," *IEEE Trans. Pattern Anal. Mach. Intell.*, vol. 44, no. 12, pp. 8992–9010, 2022.
- [46] W. Sun, C. Liu, J. Li, Y. M. Lai, and W. Li, "Low-rank and sparse matrix decomposition-based anomaly detection for hyperspectral imagery," *J. Appl. Remote Sens.*, vol. 8, no. 1, p. 83641, 2014.
- [47] E. J. Candès, X. Li, Y. Ma, and J. Wright, "Robust principal component analysis?," *J. ACM*, vol. 58, no. 3, pp. 1–37, 2011.
- [48] Y. Zhang, B. Du, L. Zhang, and S. Wang, "A low-rank and sparse matrix decomposition-based Mahalanobis distance method for hyperspectral anomaly detection," *IEEE Trans. Geosci. Remote Sens.*, vol. 54, no. 3, pp. 1376–1389, 2015.
- [49] Y. Xu, Z. Wu, J. Li, A. Plaza, and Z. Wei, "Anomaly detection in hyperspectral images based on low-rank and sparse representation," *IEEE Trans. Geosci. Remote Sens.*, vol. 54, no. 4, pp. 1990–2000, 2015.
- [50] S. Wang, X. Wang, L. Zhang, and Y. Zhong, "Auto-AD: Autonomous Hyperspectral Anomaly Detection Network Based on Fully Convolutional Autoencoder," *IEEE Trans. Geosci. Remote Sens.*, vol. 60, pp. 1–14, 2022.
- [51] T. Jiang, W. Xie, Y. Li, J. Lei, and Q. Du, "Weakly Supervised Discriminative Learning With Spectral Constrained Generative Adversarial Network for Hyperspectral Anomaly Detection," *IEEE Trans. Neural Networks Learn. Syst.*, vol. 33, no. 11, pp. 6504–6517, 2022.
- [52] S. Arisoy, N. M. Nasrabadi, and K. Kayabol, "GAN-based Hyperspectral Anomaly Detection," in *2020 28th European Signal Processing Conference (EUSIPCO)*, 2021, pp. 1891–1895.
- [53] T. Jiang, W. Xie, Y. Li, and Q. Du, "Discriminative semi-supervised generative adversarial network for hyperspectral anomaly detection," in *IGARSS 2020-2020 IEEE International Geoscience and Remote Sensing Symposium*, 2020, pp. 2420–2423.
- [54] N. Wang, B. Li, Q. Xu, and Y. Wang, "Automatic ship detection in optical remote sensing images based on anomaly detection and SPP-PCANet," *Remote Sens.*, vol. 11, no. 1, p. 47, 2018.
- [55] A. Sledz and C. Heipke, "Thermal Anomaly Detection Based on Saliency Analysis from Multimodal Imaging Sources," *ISPRS Ann. Photogramm. Remote Sens. Spat. Inf. Sci.*, vol. 1, pp. 55–64, 2021.
- [56] M. Shimoni, G. Tolt, C. Permeel, and J. Ahlberg, "Detection of vehicles in shadow areas using combined hyperspectral and lidar data," in *2011 IEEE International Geoscience and Remote Sensing Symposium*, 2011, pp. 4427–4430.
- [57] J. Li, H. Zhang, L. Zhang, and L. Ma, "Hyperspectral anomaly detection by the use of background joint sparse representation," *IEEE J. Sel. Top. Appl. Earth Obs. Remote Sens.*, vol. 8, no. 6, pp. 2523–2533, 2015.
- [58] N. Zhang, S. Ding, J. Zhang, and Y. Xue, "An overview on restricted Boltzmann machines," *Neurocomputing*, vol. 275, pp. 1186–1199, 2018.
- [59] S. Waqas Zamir *et al.*, "isaid: A large-scale dataset for instance segmentation in aerial images," in *Proceedings of the IEEE/CVF Conference on Computer Vision and Pattern Recognition Workshops*, 2019, pp. 28–37.
- [60] L. Ruff *et al.*, "Deep one-class classification," in *International conference on machine learning*, 2018, pp. 4393–4402.
- [61] E. Eban, M. Schain, A. Mackey, A. Gordon, R. Rifkin, and G. Elidan, "Scalable learning of non-decomposable objectives," in *Artificial intelligence and statistics*, 2017, pp. 832–840.
- [62] X.-L. Zhang and M. Xu, "AUC optimization for deep learning-based voice activity detection," *EURASIP J. Audio, Speech, Music Process.*, vol. 2022, no. 1, pp. 1–12, 2022.
- [63] Y. Qu *et al.*, "Hyperspectral anomaly detection through spectral unmixing and dictionary-based low-rank decomposition," *IEEE Trans. Geosci. Remote Sens.*, vol. 56, no. 8, pp. 4391–4405, 2018.
- [64] S. Mabu, K. Fujita, and T. Kuremoto, "Disaster Area Detection from Synthetic Aperture Radar Images Using Convolutional Autoencoder and One-class SVM," *J. Robot. Netw. Artif. Life*, vol. 6, no. 1, pp. 48–51, 2019.
- [65] S. Sinha *et al.*, "Variational autoencoder anomaly-detection of avalanche deposits in satellite SAR imagery," in *Proceedings of the 10th International Conference on Climate Informatics*, 2020, pp. 113–119.
- [66] C.-I. Chang, "Multiparameter receiver operating characteristic analysis for signal detection and classification," *IEEE Sens. J.*, vol. 10, no. 3, pp. 423–442, 2010.



Jingtao Li received the B.S. degree from School of Geography and Information Engineering, China University of Geosciences, Wuhan, China, in 2021. He is currently pursuing the Ph.D. degree in photogrammetry and remote sensing with State Key Laboratory of Information Engineering in Surveying, Mapping and Remote Sensing, Wuhan University. His major research interests anomaly detection in remote sensing.



Xinyu Wang received the B.S. degree in photogrammetry and remote sensing, in School of Remote Sensing and Information Engineering in 2014, and the Ph.D. degree in communication and information systems in the State Key Laboratory of Information Engineering in Surveying, Mapping and Remote Sensing (LIESMARS) in 2019, from Wuhan University, Wuhan, China. Since 2019, he has been an associate research fellow in School of Remote Sensing and Information Engineering, Wuhan University, Wuhan. His major research interests include multisource remote sensing data processing and its applications.



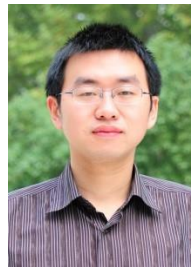
Hengwei Zhao received the B.S. degree in surveying and mapping engineering from the School of Resources and Civil Engineering, Northeastern University, ShenYang, China, in 2019. He is currently pursuing the Ph.D. degree in photogrammetry and remote sensing with the State Key Laboratory of Information Engineering in Surveying, Mapping and Remote Sensing, Wuhan University, Wuhan.



Liangpei Zhang (M'06–SM'08–F'19) received the B.S. degree in physics from Hunan Normal University, Changsha, China, in 1982, the M.S. degree in optics from the Xi'an Institute of Optics and Precision Mechanics, Chinese Academy of Sciences, Xi'an, China, in 1988, and the Ph.D. degree in photogrammetry and remote sensing from Wuhan University, Wuhan, China, in 1998.

He is a "Chang-Jiang Scholar" chair professor appointed by the ministry of education of China in state key laboratory of information engineering in surveying, mapping, and remote sensing (LIESMARS), Wuhan University. He was a principal scientist for the China state key basic research project (2011–2016) appointed by the ministry of national science and technology of China to lead the remote sensing program in China. He has published more than 700 research papers and five books. He is the Institute for Scientific Information (ISI) highly cited author. He is the holder of 30 patents. His research interests include hyperspectral remote sensing, high-resolution remote sensing, image processing, and artificial intelligence.

Dr. Zhang is a Fellow of Institute of Electrical and Electronic Engineers (IEEE) and the Institution of Engineering and Technology (IET). He was a recipient of the 2010 best paper Boeing award, the 2013 best paper ERDAS award from the American society of photogrammetry and remote sensing (ASPRS) and 2016 best paper theoretical innovation award from the international society for optics and photonics (SPIE). His research teams won the top three prizes of the IEEE GRSS 2014 Data Fusion Contest, and his students have been selected as the winners or finalists of the IEEE International Geoscience and Remote Sensing Symposium (IGARSS) student paper contest in recent years. He also serves as an associate editor or editor of more than ten international journals. Dr. Zhang is currently serving as an associate editor of the *IEEE Transactions on Geoscience and Remote Sensing*. Dr. Zhang is the founding chair of IEEE Geoscience and Remote Sensing Society (GRSS) Wuhan Chapter.



Yanfei Zhong (M'11–SM'15) received the B.S. degree in information engineering and the Ph.D. degree in photogrammetry and remote sensing from Wuhan University, China, in 2002 and 2007, respectively.

Since 2010, He has been a Full professor with the State Key Laboratory of Information Engineering in Surveying, Mapping and Remote Sensing (LIESMARS), Wuhan University, China. He organized the Intelligent Data Extraction, Analysis and Applications of Remote Sensing (RSIDEA) research group. He has published more than 100 research papers in international journals, such as *Remote Sensing of Environment*, *ISPRS Journal of Photogrammetry and Remote Sensing*, *IEEE Transactions on Geoscience and Remote Sensing*. His research interests include hyperspectral remote sensing information processing, high-resolution remote sensing image understanding, and geoscience interpretation for multisource remote sensing data and applications.

Dr. Zhong is a Fellow of the Institution of Engineering and Technology (IET). He was a recipient of the 2016 Best Paper Theoretical Innovation Award from the International Society for Optics and Photonics (SPIE). He won the Second-Place Prize in 2013 IEEE GRSS Data Fusion Contest and the Single-view Semantic 3-D Challenge of the 2019 IEEE GRSS Data Fusion Contest, respectively. He is currently serving as an Associate Editor for the *IEEE Journal of Selected Topics in Applied Earth Observations and Remote Sensing*, and the *International Journal of Remote Sensing*.